

Optical photometry and X-ray monitoring of the “Cool Algol” BD+05°706: Determination of the physical properties

Guillermo Torres¹, Jeff A. Mader², Laurence A. Marschall³, Ralph Neuhauser^{4,5}, Alaine S. Duffy^{3,1}

gtorres@cfa.harvard.edu

*** To appear in The Astronomical Journal, June 2003 ***

ABSTRACT

We present new photometric observations in the *BVRI* bands of the double-lined eclipsing binary BD+05°706 conducted over three observing seasons, as well as new X-ray observations obtained with the ROSAT satellite covering a full orbital cycle ($P = 18.9$ days). A detailed light-curve analysis of the optical data shows the system to be semidetached, confirming indications from an earlier analysis by Torres et al. (1998), with the less massive and cooler star filling its Roche lobe. The system is a member of the rare class of cool Algol systems, which are different from the “classical” Algol systems in that the mass-gaining component is also a late-type star rather than a B- or A-type star. By combining the new photometry with a reanalysis of the spectroscopic observations reported by Torres et al. (1998) we derive accurate absolute masses for the components of $M_1 = 2.633 \pm 0.028 M_\odot$ and $M_2 = 0.5412 \pm 0.0093 M_\odot$, radii of $R_1 = 7.55 \pm 0.20 R_\odot$ and $R_2 = 11.02 \pm 0.21 R_\odot$, as well as effective temperatures of 5000 ± 100 K and 4640 ± 150 K for the primary and secondary, respectively. There are obvious signs of activity (spottedness) in the optical light curve of the binary. Our X-ray light curve clearly shows the primary eclipse but not the secondary eclipse, suggesting that the primary star is the dominant source of the activity in the system. The

¹Harvard-Smithsonian Center for Astrophysics, 60 Garden St., Cambridge, MA 02138

²McDonald Observatory, Hobby-Eberly Telescope, P.O. Box 1337, State Highway 118 North, Ft. Davis, TX 79734

³Department of Physics, Gettysburg College, 300 North Washington Street, Gettysburg, PA 17325

⁴Max-Planck-Institut für extraterrestrische Physik, D-85740 Garching, Germany

⁵Astrophysikalisches Institut und Universitätssternwarte, Universität Jena, Schillergässchen 2, D-07445 Jena, Germany

depth and duration of the eclipse allow us to infer some of the properties of the X-ray emitting region around that star.

Subject headings: binaries: eclipsing — binaries: spectroscopic — stars: activity — stars: fundamental parameters — stars: individual (BD+05°706)

1. Introduction

The class of interacting binaries known as the “classical Algols” are semi-detached systems that contain a late-type giant or subgiant that fills its Roche lobe and is transferring mass onto a much more luminous and more massive B–A main sequence star. A new class of binaries has been found with properties that are similar to those of the classical Algols, except that the mass gaining component is a late-type giant or subgiant like its companion. These systems were first recognized by Popper (1992) and are now referred to as the “cool Algols.” They typically display signs of magnetic activity in the form of Ca II H+K emission, H α emission, star spots, and strong X-ray emission. Only about a dozen cool Algols are known, and many of them were mistakenly assigned to the larger group of RS CVn binaries which contain a luminous K-type primary with a fainter F–G type companion. The main difference between the cool Algols and the RS CVn systems is that the former are undergoing Roche lobe overflow, while the latter are detached (see, e.g., Popper 1980; Hall 1989).

BD+05°706 (RXJ0441.9+0537, PPM 147827, $\alpha = 4^{\text{h}}41^{\text{m}}57^{\text{s}}.64$, $\delta = +5^{\circ}36'34''.3$, J2000, $V = 9.4$) is one of the recent additions to this rare category of cool Algols, and was discovered in the course of spectroscopic follow-up observations of a sample of X-ray sources selected from the ROSAT All-Sky Survey south of the Taurus-Auriga star-forming region (Neuhäuser et al. 1997). Although that X-ray sample was originally designed to favor the detection of T Tauri stars, which are also quite active, BD+05°706 was quickly found to be of an entirely different nature. Torres et al. (1998) (hereafter Paper I) reported a double-lined spectroscopic orbital solution with a period of 18.9 days, a very small and possibly spurious eccentricity, and a mass ratio of $q = 0.21$ ($M_{\text{secondary}}/M_{\text{primary}}$), typical of the Algol systems.

The system contains two cool giants. The G8 III “primary” (the more massive star) is detached, while the K1-K2 III “secondary” has filled its critical lobe or may overflow it (Paper I). The star we have called the “secondary” is currently the larger, less massive, and cooler component, as in the classical Algols. Spectroscopic convention is used throughout this paper instead of the notation used in papers on stellar evolution, which refer to the initially more massive star as the primary. The general properties of the system were described in Paper I. Although photometry for BD+05°706 was not available at the time of that study,

eclipses were estimated to be very likely. Subsequent photometric monitoring in the optical confirmed this prediction (Marschall et al. 1998).

The general characteristics of the cool Algols are fairly well defined (see Popper 1992, and Paper I), but accurate information on individual systems is still far from complete. Only five of the members, aside from BD+05°706, have spectroscopic orbits for both components (RZ Cnc, AR Mon, RT Lac, AD Cap, and RV Lib; Popper 1976, 1991), and light curve analyses for the first three of these have yielded the absolute masses and radii necessary in order to understand their properties. The remaining five objects identified as possible members of this class (UZ Cnc, V1061 Cyg, AV Del, GU Her, and V756 Sco; Popper 1996) have very little in the way of observations and in some cases even the orbital periods are poorly known.

The high-quality spectroscopic orbit presented for BD+05°706 in Paper I, combined with the fact that the system is eclipsing, offers the opportunity to determine the absolute dimensions of the components very accurately. To that end, photometric observations in the *BVRI* system were continued after the initial report by Marschall et al. (1998). We present here a full analysis of those data, and also a re-analysis of the spectroscopic material in Paper I with improved techniques and the benefit of the additional information provided by the light-curves. The latter offer a means for evaluating subtle distortions in the Doppler measurements due to the close proximity of the stars. As a result, we are able to determine here the absolute masses of both components with uncertainties smaller than 2%, and the radii with errors smaller than 3%, which are now the best determinations for any system of the cool Algol class.

The global X-ray properties and the activity level of BD+05°706 (Ca II H and K emission, variable H α line strength) were studied in some detail in Paper I, where it was established that the hotter primary star is most likely the site of the bulk of the activity in the binary. Additional X-ray observations for the system were secured by us with the ROSAT satellite essentially over a complete 18.9-day cycle (yielding an X-ray light curve), and clearly show the primary eclipse but not the secondary eclipse. An analysis of these data is presented here as well, allowing us to obtain information about the geometry of the X-ray emitting region surrounding the active star.

2. Observational material

The photometric observations of BD+05°706 in the optical were conducted at the Gettysburg College Observatory (Gettysburg, PA) with a 16-inch f/11 Ealing Cassegrain re-

flector. The detector was a Photometrics thermoelectrically-cooled CCD camera with a front-illuminated Thompson 7896 chip with 1024×1024 pixels. BD+05°706 was observed on 94 nights during the 1997–1999 observing seasons. A total of 80, 93, 133 and 137 observations were made in the Johnson B , V , R , and I filters, respectively. The comparison and check stars used are TYC 95-1495-1 (GSC 00095-1495) and HD 29764 (GSC 00091-00262, BD+05°704, SAO 111980), respectively. Basic properties for these stars are listed in Table 1. Coverage of the primary eclipse in the B and V filters was very poor during the first two seasons (before JD 2,451,000), and therefore those data were not used in the analysis below.

The precision of an individual differential photometric measurement is estimated to be 0.010 mag, 0.010 mag, 0.009 mag, and 0.010 mag in the B , V , R , and I passbands, respectively, derived from the comparison and check stars under the assumption that they do not vary. The observations in the sense \langle variable minus comparison \rangle are listed in Table 2, Table 3, Table 4, and Table 5. The depth of the eclipses in the V band is approximately 0.52 mag for the primary minimum and 0.34 mag for the secondary. Changes in the overall brightness at the quadratures are fairly obvious from season to season. They are not unexpected given the activity level displayed by the system, and will be discussed in more detail in §3.

The spectroscopic material used here is the same as that reported in Paper I. Briefly, it consists of 41 single-order echelle spectra obtained from 1994 March to 1996 March with the 1.5-m Wyeth reflector at the Oak Ridge Observatory (Harvard, Massachusetts), the 1.5-m Tillinghast reflector at the Fred L. Whipple Observatory (Mount Hopkins, Arizona), and the Multiple Mirror Telescope (also atop Mount Hopkins, Arizona) prior to its conversion to a monolithic 6.5-m mirror. The spectra cover 45 \AA with a central wavelength of 5187 \AA , and the resolving power is $\lambda/\Delta\lambda \sim 35,000$. The reductions to obtain radial velocities for both components are slightly different from those used in Paper I, and are described later.

X-ray observations of BD+05°706 were obtained with the High Resolution Imager instrument (HRI; David et al. 1996) aboard the ROSAT satellite over a period of 18 days covering essentially a full orbital cycle of the binary, from 1997 August 18 to September 5. The measurements were made at intervals of one day, with the exception of a 3-day gap due to scheduling constraints. The exposure times were typically about 3.5 ksec each, achieving signal-to-noise (S/N) ratios ranging from 6 to 15 per broad-band observation (0.1 to 2.4 keV), with a mean S/N of 10. The observations were reduced with the Extended Scientific Analysis Software (EXSAS, Zimmermann et al. 1994) version 2001 running under ESO-MIDAS version 01FEB. In addition to considering the full energy range of ROSAT, we subsequently divided the recorded counts into a soft band including detector channels 0 through 3 (0.1 to 0.5 keV) and a hard band including channels 4 through 15 (0.6 to 2.4 keV)

in order to obtain additional information from the analysis of these data. We performed standard local and map source detection in all three spectral bands. The S/N ratios range from 4 to 10 in the soft band and from 4 to 11 in the hard band. This allows us to define a “hardness ratio” $HR = (H - S)/(H + S)$, where H and S are the hard and soft count rates, respectively (see Huélamo et al. 2000).

The individual X-ray observations are listed in Table 6. The columns give the heliocentric Julian date and the exposure times, followed by the count rates, the corresponding errors, and the Maximum Likelihood (ML) estimator for the soft, hard, and broad bands (Cruddace, Hasinger & Schmitt 1988). The quantity ML provides a measure of the existence of the source above the local background. For example, a Maximum Likelihood of 7.4 (14.3) corresponds to a 3.5σ (5σ) detection. The last three columns give the hardness ratio and its corresponding uncertainty, as well as the phase in the orbit of the binary⁶.

Figure 1 shows the time history of the optical photometry, the spectroscopy, and the X-ray observations. Because of the variability of the object, the time coverage of the optical light curves and the radial velocities is relevant for the modeling of the system, as we describe in §4. In the analyses below all data were phased with the ephemeris

$$\text{Min I} = \text{HJD } 2,449,924.582 (\pm 0.012) + 18.8988 (\pm 0.0011) \times E, \quad (1)$$

where the epoch refers to the time of primary eclipse (more massive star occulted by the other star), and E is the number of cycles counted from this epoch. This ephemeris was determined from the radial velocity observations described in §4, and supersedes the one given in Paper I.

3. Analysis of the optical photometry

Examination of the raw light curves for BD+05°706 revealed significant changes over the three observing seasons that precluded their merging into a single data set for analysis. The extent of the changes is such that, for example, during the 1997–1998 season the light level in the V band at the first quadrature was lower than at the second quadrature, whereas by the following season the situation had reversed. Variations of this nature are common in active systems, and are well explained by the presence of surface features (spots) on

⁶Since the soft-, hard-, and broad-band counts are computed separately by the Maximum Likelihood detection algorithm, the soft and hard counts in Table 6 do not exactly add up to the broad-band counts, although the difference is minimal. The mean local background is estimated separately in each band and then subtracted from the corresponding total counts, which contributes to the slight discrepancy.

one or both stars. In order to minimize the scatter, a compromise between the number of observations, the completeness of the phase coverage (particularly at the minima), and the intrinsic variations was made by dividing the observations into two data sets at Julian Date 2,451,000 (see Figure 1). As mentioned above, the measurements in the B and V filters in data set #1 do not cover the primary eclipse, and they were therefore not used for the final fits. Light curve analyses were carried out separately for each bandpass in each data set (RI for data set #1, and $BVRI$ for data set #2), and also for the combined data.

The light curve solutions were performed with the Wilson-Devinney code (Wilson & Devinney 1971; Wilson 1979, 1990) in a mode appropriate for semi-detached systems, in accordance with the information available for the stars from Paper I. Specifically, we used “Mode 5” for a secondary that is filling its limiting lobe. Detached and overcontact configurations were tried as well, but the solutions were never as satisfactory as those in the semi-detached mode. They always converged towards the secondary star filling its Roche lobe and the primary well within its critical surface, in agreement with the assessment in Paper I. Solutions were found for the modified gravitational potential of the primary (Ω_1 , in the Wilson-Devinney usage), the inclination angle (i), the relative monochromatic luminosity of the primary (L_1), the mean temperature of the secondary (T_2), and a phase offset ($\Delta\phi$). The temperature of the primary was held fixed at the spectroscopic value of $T_1 = 5000$ K, as was the mass ratio $q \equiv M_2/M_1 = 0.2055$ (see §4). We have assumed the orbit to be circular, consistent with the results of the new spectroscopic analysis below. The monochromatic luminosity of the secondary (L_2) was computed by the program directly from the temperatures of the primary and secondary, the luminosity of the primary, the radiation laws, and the geometry of the system. Limb-darkening coefficients were interpolated from the tables by van Hamme (1993) for the appropriate temperatures and for surface gravities of $\log g_1 = 3.0$ and $\log g_2 = 2.0$ (see §4). A value of 0.5 was adopted for the bolometric albedo of both components, appropriate for stars with convective envelopes. Gravity brightening coefficients were interpolated from the models by Claret (2000).

Aside from the usual light elements, the distortions mentioned above in the light curves suggested the presence of one or more spots requiring additional free parameters. The Wilson-Devinney code is capable of accounting for spots (assumed to be circular in shape) based on a simple representation with four additional parameters: the longitude (l , in degrees) measured counter-clockwise (as seen from above) from the line joining the centers of the stars, the latitude (b , in degrees), the angular radius (r , in degrees), and a temperature factor ($TF = T_{\text{spot}}/T_{\text{star}}$) representing the contrast in temperature between the spot and the surrounding photosphere.

Numerical experiments showed that in our case the fits cannot usually distinguish the

component on which the spots are located, since similarly good solutions resulted with the spots on either star. In the RS CVn systems the spots are typically located on the cooler star, which is usually the more active component. There are a number of cases, however, in which the spots have instead been shown to be on the hotter star (e.g., Hill, Fischer & Holmgren 1990; Vivekananda Rao, Sarma & Prakash Rao 1991; Kjurkchieva, Marchev & Ogloza 2000; Albayrak et al. 2001). In BD+05°706 there are strong indications that the activity is in fact associated with the hotter star (the primary), as evidenced by the H α emission (see Paper I) and also the X-ray properties discussed later in §6. It is therefore not unreasonable to assume in the following that the spottedness in this system is primarily associated with the hotter star. More complicated models with spots on both stars are possible, but are probably not justified given the data available.

The maximum brightness outside of eclipse is much the same for data sets #1 and #2, although it occurs at phase 0.75 in the first set and at phase 0.25 in the second. The lower brightness levels at the other quadrature in each data set are not quite as similar to each other and show more scatter in the photometric observations. This suggests that the lower light levels may be due to one or more cool spots (which tend to change with time in other similarly active stars), as opposed to hot spots being the cause of the higher brightness at the other quadratures. Spots that are cooler than the photosphere have typically been found also in virtually all RS CVn systems (although warm features have been reported in a few cases; see, e.g., Strassmeier & Rice 2003). Thus we will assume here that the spots are cool. The situation for BD+05°706 obviously calls for the cool spots to be located at roughly opposite longitudes in the two epochs, and we found that a single spot at each epoch gave an adequate representation of the light curves, within the observational errors.

Further tests showed that, due to the strong correlation between the size and temperature of the spots, it was not possible to determine both simultaneously from the observations at our disposal. Grids of preliminary solutions at fixed values of TF from 0.5 to 1.0 indicated a slight preference for a spot in data set #1 with $TF = 0.84$ (800 K cooler than the photosphere), and a similar spot in data set #2 with $TF = 0.87$ (650 K cooler than the photosphere). These values are within the typical range seen in other RS CVn binaries (O’Neal, Saar & Neff 1996; Schrijver 2002). Therefore, in the following we have held TF fixed at these values, and the spot radius was left free.

We also found that the sensitivity of the solutions to the latitude of the spot is very weak. Experiments with fixed values of b from 0° to 90° indicated only a very slight preference for mid-latitude features, with fits at higher or lower latitudes being almost indistinguishable. Although spots on the Sun are usually found at low latitudes, Doppler imaging studies have shown that RS CVn systems tend to display high-latitude features and even spots that

straddle the pole (e.g., Hatzes 1995; Vogt et al. 1999). While BD+05°706 is similar to the RS CVn binaries in many respects, the latter systems typically rotate much more rapidly (see, e.g., Strassmeier 2002). Theoretical studies suggest that rapid rotation in convective stars leads to the emergence of spots at higher latitudes (Schüssler & Solanki 1992; Schüssler et al. 1996; Granzer et al. 2000), and there is some observational support for this trend (see Hatzes 1998). Therefore, for this study we have adopted a fixed latitude of 45°, in agreement with the above and also with the theoretical work by Granzer (2002) that focuses specifically on evolved stars similar to those in BD+05°706.

Initially light curve solutions were obtained separately for each bandpass in each data set (*RI* for data set #1, and *BVRI* for data set #2), to evaluate the consistency between them. The results were found to be reasonably similar, except that the second data set showed a larger scatter in the temperature of the secondary (T_2) and in the potential of the primary (Ω_1). Solutions were also obtained from the combined *RI* and *BVRI* observations from data sets #1 and #2, respectively, which were also quite similar to each other. Since the main geometric properties (Ω_1 and i) are not expected to change from season to season, the results for these two parameters from the two data sets were averaged (with weights proportional to the internal errors), and fixed in subsequent analyses. We then repeated the fits and computed the average secondary temperature ($T_2 = 4638$ K) from the simultaneous multi-band analyses. Finally, we fixed T_2 to this value, and we solved for the remaining parameters including the size (r) and longitude (l) of the spots, which clearly do change with time. The results are given in Table 7 and Table 8 for data set #1 and #2, respectively. We show the separate fits for each filter before fixing any of the parameters, and also the simultaneous multi-band analyses in the last column calculated with Ω_1 , i , and T_2 set to their average values. Also listed are the fractional radii (r_{point} , r_{pole} , r_{side} , r_{back} , in terms of the separation) as well as the relative radius of a spherical star with the same volume as the distorted stars (r_{vol}), for the primary and secondary. The uncertainties given in these tables are standard errors as reported by the Wilson-Devinney code. Experiments were also carried out to explore the significance of third light (L_3), but in all cases the results were consistent with $L_3 = 0$.

Both eclipses in BD+05°706 are partial, with approximately 65% of the light of the primary being blocked at phase 0.0. The latter star is nearly spherical in shape since the difference between its polar radius and the radius directed towards the inner Lagrangian point is less than 0.5%. Parameters r_{point} , r_{pole} , r_{side} , and r_{back} in Table 7 and Table 8 confirm that the secondary is distorted because it fills its Roche lobe.

A graphical representation of the observations and light curve solutions is given in Figure 2 and Figure 3 for data sets #1 and #2. The $O - C$ residuals are shown at the

bottom for each passband. The B and V light curves in data set #1 lack coverage at the primary minimum, and do not allow one to determine any of the parameters reliably. Although we show them here for completeness, these observations were not used in any of the fits described above. For these B and V solutions all geometric and radiative parameters as well as the spot parameters were adopted from the combined RI solution, and only the primary luminosity was allowed to vary. The fits are consequently poorer.

The spots that were found to provide a good fit to the observations in both data sets are represented in Figure 4, with the size and separation of the stars shown to scale. The difference in longitude between one epoch and the other (separated by approximately 1.4 years) is about 140° . The surface area covered by the spots is in line with what is seen in other active systems, and reaches $\sim 20\%$ of one hemisphere of the primary star in data set #1, and $\sim 17\%$ in data set #2.

4. Spectroscopic analysis

The procedures used here for the reduction of the spectroscopic material are similar to those described in Paper I in that we derived radial velocities for the two components using TODCOR (Zucker & Mazeh 1994), a two-dimensional cross-correlation technique well suited to our relatively low S/N spectra. However, a number of improvements were introduced that justified a re-analysis of the original data. First, we now have at our disposal a new library of synthetic spectra based on more recent model atmospheres by R. L. Kurucz⁷, which provide a somewhat better match to the spectra of real stars. The use of these new templates has a small effect on the temperature and rotational velocity ($v \sin i$) derived for the components of BD+05°706, and can potentially affect the radial velocities as well.

We re-determined the $v \sin i$ values by running extensive grids of correlations as described in Paper I. The results were $v_1 \sin i = 23 \text{ km s}^{-1}$ and $v_2 \sin i = 31 \text{ km s}^{-1}$, with estimated errors of 1 km s^{-1} and 2 km s^{-1} , respectively. The primary value is 1 km s^{-1} larger than in Paper I, and the secondary value is unchanged. The new effective temperatures, derived from similar grids, were $T_1 = 5000 \text{ K}$ and $T_2 = 4600 \text{ K}$, with uncertainties of 100 K . These differ by less than 100 K from the determinations in Paper I. The new primary value was adopted for the light curve solutions described above.

A second improvement has to do with residual systematic errors in the raw velocities, mostly due to the relatively narrow spectral window of these observations. Experience with

⁷Available at <http://cfaku5.cfa.harvard.edu>.

similar spectroscopic material for other binary systems has shown that these errors can be quite significant in some cases (Torres et al. 1997, 1999; Lacy et al. 2000). We have investigated these errors for the present system by means of numerical simulations that were discussed in detail by Latham et al. (1996). Briefly, we generated a set of artificial binary spectra by combining the primary and secondary templates in the appropriate ratio and applying velocity shifts for both components as computed from a preliminary orbital solution at the actual times of observation of each of our spectra. These artificial spectra were then processed with TODCOR in exactly the same way as the real observations, and the resulting velocities were compared with the input (synthetic) values. The differences $\langle \text{TODCOR} \text{ minus synthetic} \rangle$ are typically under 0.5 km s^{-1} , but they are systematic in nature. Even though the effect on the masses is relatively small in this particular case, we have nevertheless applied these differences as corrections to the measured velocities of BD+05°706. The corrected velocities are listed in Table 9 (columns 2 and 3). The differences with the values reported in Paper I are generally below 1 km s^{-1} .

As a result of the proximity and distorted shapes of the stars (see, e.g., Figure 4), the radial velocities measured for the components of BD+05°706 are biased to some extent because of the loss of symmetry in the intensity distribution across the disks of the stars. In addition, the observations collected during the eclipses suffer from the well-known Rossiter effect (Rossiter 1924; McLaughlin 1924), which depends on the rotation rate. The combined magnitude of these two effects on the measured velocities, computed with the aid of the Wilson-Devinney program, is illustrated in Figure 5. The change in the primary velocities is essentially confined to the eclipses (and is mostly due to the Rossiter effect since that star is not far from the spherical shape), but the secondary velocities show changes throughout the entire orbital cycle because of the highly distorted shape of the Roche-lobe filling star. The corrections for the case of BD+05°706 can reach values as large as 4 km s^{-1} , and are listed in columns 4 and 5 of Table 9. The final values for the radial velocities used below, after applying these adjustments, are given in columns 6 and 7.

While the corrections described in the preceding paragraph (which depend only on the geometry of the system) do not change with time, the surface features modeled in the light curves, which can also affect the measured velocities, do change significantly as seen in §3. Spots have an effect on the measured velocities because they too contribute to break the symmetry of the intensity distribution on the stellar disks. In this case the effect will be on the primary velocities because the spots are assumed to be on that star. The phase dependence of the effect is seen in Figure 6 separately for data sets #1 and #2, and was derived once again using the Wilson-Devinney code. Specifically, the effect is calculated as the difference between the velocities from purely Keplerian motion and those computed by integration over the visible disk of the star, with its non-uniform brightness distribution due to the spots.

It is unclear whether the velocities we have measured by cross-correlation are affected by the full amplitude of the correction computed by this program, but presumably they will be biased to some extent in the direction indicated. Unfortunately, as seen in Figure 1 our spectroscopic observations were not simultaneous with either of the photometric data sets, so that corrections for this effect cannot be applied. The magnitude of the distortion in the velocities can reach values as large as 1 km s^{-1} (Figure 6). Nevertheless, as a test we applied these corrections to our velocities separately for both data sets and recomputed the spectroscopic orbit to explore the impact on the elements. For data set #1 the changes in all derived quantities including the minimum masses are of the order of 1σ or smaller. For data set #2 they are less than 0.5σ .

Our final spectroscopic orbital solution was obtained using the measured velocities corrected for proximity effects and for the Rossiter distortions only. The minimum masses and the mass ratio we determine are only slightly different from those reported in Paper I, but we now find that the eccentricity is indistinguishable from zero. The original solution in Paper I gave a value of $e = 0.0141 \pm 0.0026$, more than 5σ different from zero. This presented something of a puzzle given that tidal forces for stars with deep convective envelopes such as those in BD+05°706 are expected to circularize the orbit very quickly for the relatively short period in this system, considering that both components are giants. The distortion corrections applied here appear to have solved this dilemma, and a circular orbit is adopted hereafter.

The revised elements of the spectroscopic orbit are given in Table 10. The ephemeris for the primary eclipse that we derive from this orbit is that given in eq.(1), and was adopted for the light-curve solutions. The light ratio at the wavelength of our observations (5187 \AA), computed as described by Zucker & Mazeh (1994), is $L_2/L_1 = 1.06 \pm 0.03$. A slight correction of $+0.06$ is required to convert this to the visual band (see Paper I). The residuals of the individual observations from the orbital fit are listed in columns 8 and 9 of Table 9.

5. Absolute dimensions

The light elements in the last column of Table 7 and Table 8 combined with the spectroscopic elements in Table 10 lead to the absolute masses and radii of the components, along with other derived properties. As mentioned earlier, the uncertainties listed for the light elements are strictly internal errors reported by the Wilson-Devinney code. More realistic errors for the inclination angle, the primary and secondary potentials, and for the secondary temperature were adopted based in part on the agreement between the solutions in the different passbands and on the sensitivity of the fits to the various parameters: $i = 79^\circ 47 \pm 0^\circ 15$,

$\Omega_1 = 6.03 \pm 0.15$, $\Omega_2 = 2.246 \pm 0.011$, and $T_2 = 4640 \pm 150$ K. The physical properties of the stars are summarized in Table 11.

The absolute masses are determined with errors of 1.0% and 1.7% for the primary and secondary, respectively, while the radii are good to 2.6% and 1.9%. Since the difference in the depths of the minima is a very sensitive indicator of the temperature difference between the components, the later quantity is typically best determined from the light curves. In this case the result ($\Delta T_{\text{eff}} = 360$ K) is in excellent agreement with our spectroscopic determination of $\Delta T_{\text{eff}} = 400$ K inferred in §4, based on grids of cross-correlations with synthetic spectra. The ratio of the luminosities in the visual band from the light curve solutions is $(L_2/L_1)_V = 1.44 \pm 0.05$, whereas the estimate derived from the bolometric luminosities and bolometric corrections (Table 11) is $(L_2/L_1)_V = 1.29 \pm 0.26$. The first of these values is larger than the spectroscopic estimate [$(L_2/L_1)_V = 1.12 \pm 0.03$], a discrepancy possibly related to the presence of spots.

The measured projected rotational velocity of the secondary component, $v_2 \sin i$, is consistent with the predicted value for synchronous rotation within the errors, as expected from the fact that the star is filling its critical surface. On the other hand, the rotation of the primary is formally some 15% faster than the predicted value, a 2.8σ difference that may perhaps be significant. The primaries of many other Algol systems have also been found to rotate supersynchronously, and in some cases even close to the centrifugal limit (see, e.g., van Hamme & Wilson 1990). This spin-up is usually explained by angular momentum transfer through accretion (Huang 1966).

The inferred distance to BD+05°706 of 595 ± 51 pc relies on the apparent brightness of the system ($V = 9.45 \pm 0.03$), the interstellar extinction adopted in Paper I ($A_V = 0.35 \pm 0.15$), and bolometric corrections from Flower (1996).

6. X-ray light curve

The count rates over the full spectral range (0.1–2.4 keV) of the X-ray observations of BD+05°706 carried out with the ROSAT satellite are shown as a function of orbital phase in Figure 7a. Two features of this broad-band light curve are immediately obvious: (a) While the primary eclipse is clearly present, there is no sign of a secondary eclipse near phase 0.5; (b) One measurement immediately preceding phase 0.5 and another one following it are about a factor of two higher than the average level of the neighboring points.

The first of these features supports the notion that the primary is the X-ray active star in the system, and that the secondary contributes little, if anything, to the total X-ray

luminosity of the binary. This observation is consistent with the activity evidence presented in Paper I, where the primary was shown to be the dominant source of the $H\alpha$ emission. As reported there, several red spectra of the binary outside of eclipse displayed relatively weak $H\alpha$ absorption (residual intensity ≈ 0.8), whereas one spectrum obtained during primary eclipse displayed a much deeper $H\alpha$ line (residual intensity ≈ 0.2). This change was interpreted as an indication that the emission from the active primary fills in the normal absorption line of the secondary at most phases in the orbit making it appear weak, except near phase 0.0, where the primary is blocked and the secondary dominates the spectrum.

The second feature —unusually large X-ray flux of the two observations near phase 0.5— could possibly be due to two separate flaring events, which would not be uncommon in this type of system. We discuss this further below.

A comparison with the light curves in the optical reveals two other notable characteristics of the X-ray light curve: (c) The duration of the primary eclipse in X-rays is much longer than in the optical; (d) The primary minimum is considerably deeper in X-rays than it is in the optical. To illustrate these two features we have superimposed on Figure 7a the light curve in the R band from data set #1, which is contemporaneous with the ROSAT observations. The optical light curve is normalized to agree with the average level of the X-ray curve outside of eclipse. We note that at the epoch of these observations the configuration of the system inferred in §3 includes a cool spot on the primary that is on the far side of the star at phase 0.75 and therefore does not affect the R -band light curve at the second quadrature. The solid line in Figure 7a represents the modeled R -band light curve without the effect of the spot, and the dotted line includes the distortion due to the spot, which makes the system fainter at the first quadrature.

It can be seen from the figure that the total duration of the primary eclipse in the optical is approximately 0.11 in phase (~ 2.1 d), while the duration in X-rays is roughly 2.9 times longer (~ 0.32 in phase, or ~ 6.0 d). This implies that the size of the X-ray emitting region around the primary must be larger than the star itself by approximately the same factor. Since the radius of the star in terms of the separation is $R_1/a = 0.1720$ (parameter r_{vol} in Table 7), it follows that the radius of the associated X-ray region is $R_X/a \approx 0.50$. We note also that the mass ratio of the binary leads independently to a mean radius for the critical surface of the primary of $R_1^{\text{Roche}}/a = 0.53$. Thus, the size of the X-ray emitting region around the primary happens to be very close to that of its Roche lobe —possibly not a coincidence— and one may speculate that the X-ray emitting plasma is perhaps contained within the critical surface. Since there is no evidence from the X-ray light curve of any significant emission from the secondary, one might also speculate that the coronal region around that component represents a relatively thin layer that does not extend significantly

above the photosphere of the star, which already fills its Roche lobe. As a result, BD+05°706 would appear to exhibit the curious property of being essentially an overcontact system in X-rays, and a semidetached system in the optical⁸.

At optical wavelengths (R band) the brightness of BD+05°706 during the primary minimum drops to about 62% of the level outside of eclipse (phase 0.75). In X-rays the eclipse is much deeper, reaching down to $\sim 30\%$ of maximum. Since blocking by the same star (the secondary) produces significantly different depths in the optical and in X-rays, and given that the apparent size of the primary in X-rays is much larger, one possible explanation for the deeper minimum than in the optical may be that the X-ray brightness distribution on the primary is considerably more concentrated towards the center of the disk (or toward the inner Lagrangian point, which is projected not far from the center) than in the optical. In order to simulate this situation with light-curve solution programs such as Wilson-Devinney, not originally intended for this type of problem, the relative sizes of the stars must be changed compared to the geometry inferred from the optical light curves, effectively by altering the mass ratio. Furthermore, variations in the predicted light curve near phase 0.5 due to the changing aspect ratio of the primary (if it is assumed to fill its critical surface in X-rays) must be ignored as they probably do not apply at X-ray wavelengths. We find a reasonably good agreement between such a “model” and the observed light curve when the effective size of the X-ray emitting region of the primary is reduced to approximately the same size as the photosphere of the lobe-filling secondary (see Figure 7b). Of course, any parameters derived in this way are physically meaningless and are only intended to achieve a qualitatively good fit. The reference provided by this very crude model does seem to suggest, nevertheless, that the X-ray flux preceding the primary eclipse (beginning at phase 0.75, and perhaps including the descending branch) is somewhat lower than the flux after the minimum at symmetrical phases.

As mentioned above, the two high X-ray points near phase 0.5 might be due to two separate flare events (since an observation intermediate between these two shows a normal flux level). X-ray flares are common in RS CVn systems (see, e.g., Siarkowski et al. 1996; García-Alvarez et al. 2003). On the other hand, the semidetached configuration in the optical is an indication that mass transfer by Roche-lobe overflow may be occurring. Due to the relatively large size of the primary, a stream of material from the secondary to the primary would actually impact the primary star directly rather than sweep past it and form a disk (Lubow & Shu 1975, see also Figure 11 in Paper I). Given the orbital phases at which the discrepant X-ray points in Figure 7a occur (0.423 and 0.539), just before and just after

⁸For an illuminating discussion of the meaning of the word “overcontact”, we refer the reader to the recent papers by Rucinski (1997) and Wilson (2001).

central blocking of the secondary by the primary, it is possible that the sudden increase in X-ray flux is related to the viewing angle of the stream associated with mass transfer, which would be roughly aligned with the line of sight at these phases. Detailed hydrodynamical modeling is required to investigate this further.

In Figure 8 we have split the ROSAT X-ray observations of BD+05°706 into a soft band (0.1–0.5 keV) and a hard band (0.6–2.4 keV) in order to investigate the possibility that there might be a difference in the behavior as a function of orbital phase. The run of the count rates turns out to be quite similar, however, with the soft band being slightly lower throughout (Figure 8a). The changes in the hardness ratio as defined in §2 are shown in Figure 8b. Within the errors the HR values are fairly constant, the decrease toward the primary minimum being only marginally significant. In particular, the observations near phase 0.5 pointed out in the broad-band light curve (Figure 7a) that are possibly associated with flaring episodes show no sign that the X-ray energy becomes significantly harder (observations marked with circles), as would be expected if the temperature were to increase due to heating of the plasma.

7. Discussion and concluding remarks

The combination of our new $BVRI$ photometry with a reanalysis of the spectroscopy reported in Paper I has allowed us to obtain highly precise absolute masses and radii for both components of the semidetached system BD+05°706, as well as the effective temperatures and other properties. Among the dozen or so known cool Algols, this is now by far the one with the best determined physical parameters. Only three others have published light-curve solutions to date (RZ Cnc, AR Mon, and RV Lib).

In Paper I the eclipsing nature of BD+05°706 was not yet known, so there was no direct information on the orbital inclination angle although some constraints were available based on other evidence. Qualitative conclusions on the history and evolutionary state of the system were drawn there based upon the assumption that the inclination angle was large, and therefore that the true values of the masses and the radii were not far from the lower limits derived for those quantities. We can now confirm the validity of that assumption in Paper I, and consequently also of those conclusions: the present configuration of BD+05°706 was probably reached as a result of Case B mass transfer (Kippenhahn & Weigert 1967), and the initial mass ratio of the system is likely to have been close to unity (see Eggleton 1992; Nelson & Eggleton 2001) so that the original secondary had enough time to begin its evolution off the main sequence before the original primary reached the point of Roche-lobe overflow and started transferring mass onto it (eventually leading to a mass ratio reversal).

The minimum amount of mass exchanged (under conservative mass transfer) is $\Delta M = M_1 - (M_1 + M_2)/2 = 1.05 M_\odot$. Thus, the secondary appears to have lost at least 2/3 of its original mass. As noted in our earlier study of this system, although the current mass ratio ($q \approx 0.21$) is quite typical of classical Algol systems the relatively cool temperature of the current primary (5000 K) is not. This difference with the much hotter primaries of the classical Algols is at least qualitatively well explained by the ideas about the evolution of cool Algols mentioned above and discussed at length in Paper I.

Evidence from our optical light curves suggests the presence of large surface inhomogeneities (spots) which are quite common in similarly active systems. Significant shifts in the location (longitude) of these features are seen in BD+05°706 over a period of 1-2 years, which are also consistent with changes seen in other RS CVn binaries. Our X-ray light curve showing only the primary eclipse confirms the report in Paper I that the hotter and more massive primary star is the dominant site of activity in this binary. It is interesting to note that this is not typically the case in RS CVn systems, where the cooler star is usually the more magnetically active component. The X-ray observations also offer interesting clues about the geometry and other properties of the X-ray emitting region, which may be confined to the size of the critical lobe of the current primary star.

Photometric and spectroscopic studies of other binaries systems identified as cool Algols are currently underway as part of a long-term project to study this very interesting class of active stars. Detailed analyses of those cases along the lines of the one presented here for BD+05°706 are expected to provide further glimpses into their properties and evolutionary histories.

We thank the anonymous referee for numerous comments and helpful suggestions. This research has made use of the SIMBAD database, operated at CDS, Strasbourg, France, and of NASA’s Astrophysics Data System Abstract Service. RN wishes to acknowledge financial support from the Bundesministerium für Bildung und Forschung through the Deutsche Zentrum für Luft- und Raumfahrt e.V. (DLR) under grant number 50 OR 0003. LM would like to acknowledge the help of Julia Lynch and Akbar Rizvi in making these observations. The Gettysburg College Observatory is supported by Gettysburg College with additional funding for the CCD camera provided by the National Science Foundation.

REFERENCES

- Albayrak, B., Demircan, O., Djurašević, G., Erkapić, S., & Ak, H. 2001, *A&A*, 376, 158
- Claret, A. 2000, *A&A*, 359, 289
- Cruddace R. G., Hasinger G. R., Schmitt J. H. M. M. 1988, in *Astronomy From Large Databases*, ESO Conference and Workshop Proc. 28, eds. F. Murtagh & A. Heck (Garching), p. 177
- David, L. P., Harnden, F. R., Kearns, K. E., & Zombeck, M. V. 1996, *The ROSAT High Resolution Imager Calibration Report*, SAO Technical Report, p. 6
- Eggleton, P. P. 1992, in *IAU Symp. 151, Evolutionary Processes in Interacting Binary Stars*, ed. Y. Kondo, R. F. Sisteró, & R. S. Polidan (Dordrecht: Kluwer), 167
- Flower, P. J. 1996, *ApJ*, 469, 355
- García-Alvarez, D., Foing, B. H., Montes, D., Oliveira, J., Doyle, J. G., Messina, S., Lanza, A. F., Rodonò, M., Abbott, J., Ash, T. D. C., Baldry, I. K., Bedding, T. R., Buckley, D. A. H., Cami, J., Cao, H., Catala, C., Cheng, K. P., Domiciano de Souza Jr., A., Donati, J. F., Hubert, A. M., Janot-Pacheco, E., Hao, J. X., Kaper, L., Kaufer, A., Leister, N. V., Neff, J. E., Neiner, C., Orlando, S., O’Toole, S. J., Schäfer, D., Smartt, S. J., Stahl, O., Telting, J., & Tubbesing, S. 2003, *A&A*, 397, 285
- Granzer, Th. 2002, *AN*, 323, 395
- Granzer, Th., Schüssler, M., Caligari, P., & Strassmeier, K. G. 2000, *A&A*, 355, 1087
- Hall, D. S. 1989, in *IAU Coll. 107, Algols*, *Sp. Sc. Rev.* 50, ed. A. H. Batten (Dordrecht: Kluwer), 219
- Hatzes, A. P. 1995, *AJ*, 109, 350
- Hatzes, A. P. 1998, *A&A*, 330, 541
- Hill, G., Fischer, W. A., & Holmgren, D. 1990, *A&A*, 238, 145
- Huang, S.-S. 1966, *AJ*, 71, 165
- Huélamo, N., Neuhäuser, R., Stelzer, B., Supper, R., & Zinnecker, H. 2000, *A&A*, 359, 227
- Kippenhahn, R., & Weigert, A. 1967, *Z. Astrophys.*, 65, 251
- Kjurkchieva, D., Marchev, D., & Ogloza, W. 2000, *A&A*, 354, 909

- Lacy, C. H. S., Torres, G., Claret, A., Stefanik, R. P., Latham, D. W., & Sabby, J. A. 2000, *AJ*, 119, 1389
- Latham, D. W., Nordström, B., Andersen, J., Torres, G., Stefanik, R. P., Thaller, M., & Bester, M. 1996, *A&A*, 314, 864
- Lubow, S. H., & Shu, F. H. 1975, *ApJ*, 198, 383
- Marschall, L. A., Torres, G., & Neuhäuser, R. 1998, *BAAS*, 30, 835
- McLaughlin, D. B. 1924, *ApJ*, 60, 22
- Nelson, C. A., & Eggleton, P. P. 2001, *ApJ*, 552, 664
- Neuhäuser, R., Torres, G., Sterzik, M. F. & Randich, S. 1997, *A&A*, 325, 647
- O’Neal, D., Saar, S. H., Neff, J. E. 1996, *ApJ*, 463, 766
- Popper, D. M. 1976, *ApJ*, 208, 142
- Popper, D. M. 1980, in *IAU Symp. 88, Close Binary Stars: Observations and Interpretations*, ed. M. J. Plavec, D. M. Popper & R. K. Ulrich (Dordrecht: Reidel), 387
- Popper, D. M. 1991, *AJ*, 101, 220
- Popper, D. M. 1992, in *IAU Symp. 151, Evolutionary Processes in Interacting Binary Stars*, ed. Y. Kondo, R. F. Sisteró, & R. S. Polidan (Dordrecht: Kluwer), 395
- Popper, D. M. 1996, *ApJS*, 106, 133
- Rossiter, R. A. 1924, *ApJ*, 60, 15
- Rucinski, S. M. 1997, *IBVS* 4460
- Schrijver, C. J. 2002, *AN*, 323, 157
- Schüssler, M., Caligari, P., Ferriz-Mas, A., Solanki, S. K., & Stix, M. 1996, *A&A*, 314, 503
- Schüssler, M., & Solanki, S. K. 1992, *A&A*, 264, L13
- Siarkowski, M., Preś, P., Drake, S. A., White, N. E., & Singh, K. P. 1996, *ApJ*, 473, 470
- Strassmeier, K. G. 2002, *AN*, 323, 309
- Strassmeier, K. G., & Rice, J. B. 2003, *A&A*, 399, 315

- Torres, G., Lacy, C. H. S., Claret, A., Zakirov, M. M., Arzumanyants, G. C., Bayramov, N., Hojaev, A. S., Stefanik, R. P., Latham, D. W., & Sabby, J. A. 1999, *AJ*, 118, 1831
- Torres, G., Neuhäuser, R., & Wichmann, R. 1998, *AJ*, 115, 2028 (Paper I)
- Torres, G., Stefanik, R. P., Andersen, J., Nordström, B., Latham, D. W., & Clausen, J. V. 1997, *AJ*, 114, 2764
- van Hamme, W. 1993, *AJ*, 106, 1096
- van Hamme, W., & Wilson, R. E. 1990, *AJ*, 100, 1981
- Vivekananda Rao, P., Sarma, M. B. K., & Prakash Rao, B. V. N. S. 1991, *Journal of Astrophysics and Astronomy*, 12, 225
- Vogt, S. S., Hatzes, A. P., Misch, A. A., & Kürster, M. 1999, *ApJ*, 121, 547
- Wilson, R. E. 1979, *ApJ*, 234, 1054
- Wilson, R. E. 1990, *ApJ*, 356, 613
- Wilson, R. E. 2001, *IBVS* 5076
- Wilson, R. E., & Devinney, E. J. 1971, *ApJ*, 166, 605
- Zimmermann H. U., Becker W., Belloni T., et al. 1994, *EXSAS Users's Guide*, MPE Report 257, ROSAT Scientific Data Center, Garching
- Zucker, S., & Mazeh, T. 1994, *ApJ*, 420, 806

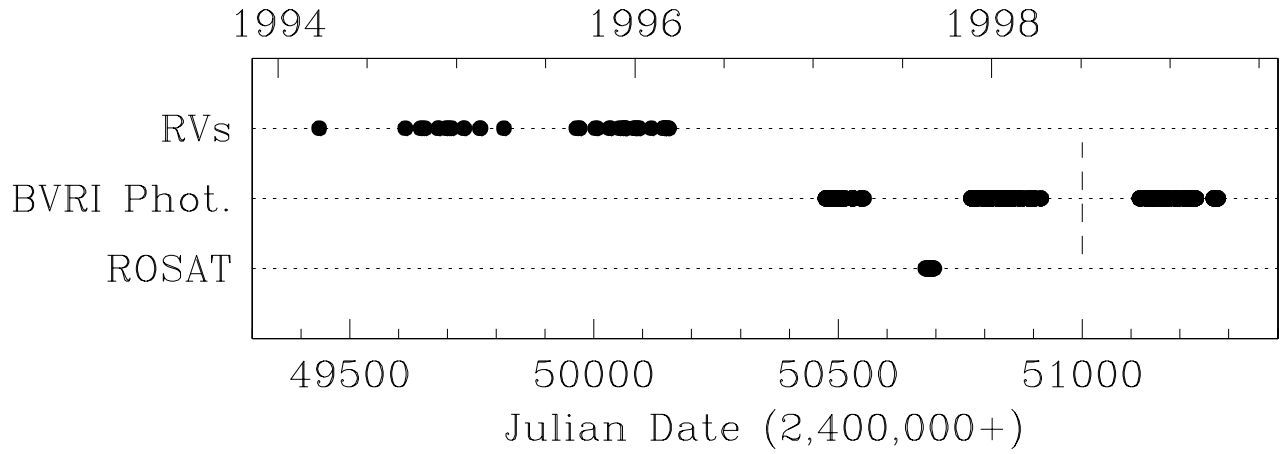


Fig. 1.— Time distribution of our spectroscopic, photometric, and X-ray observations of BD+05°706. The vertical dashed line indicates how we have divided the optical photometry measurements for analysis (see text).

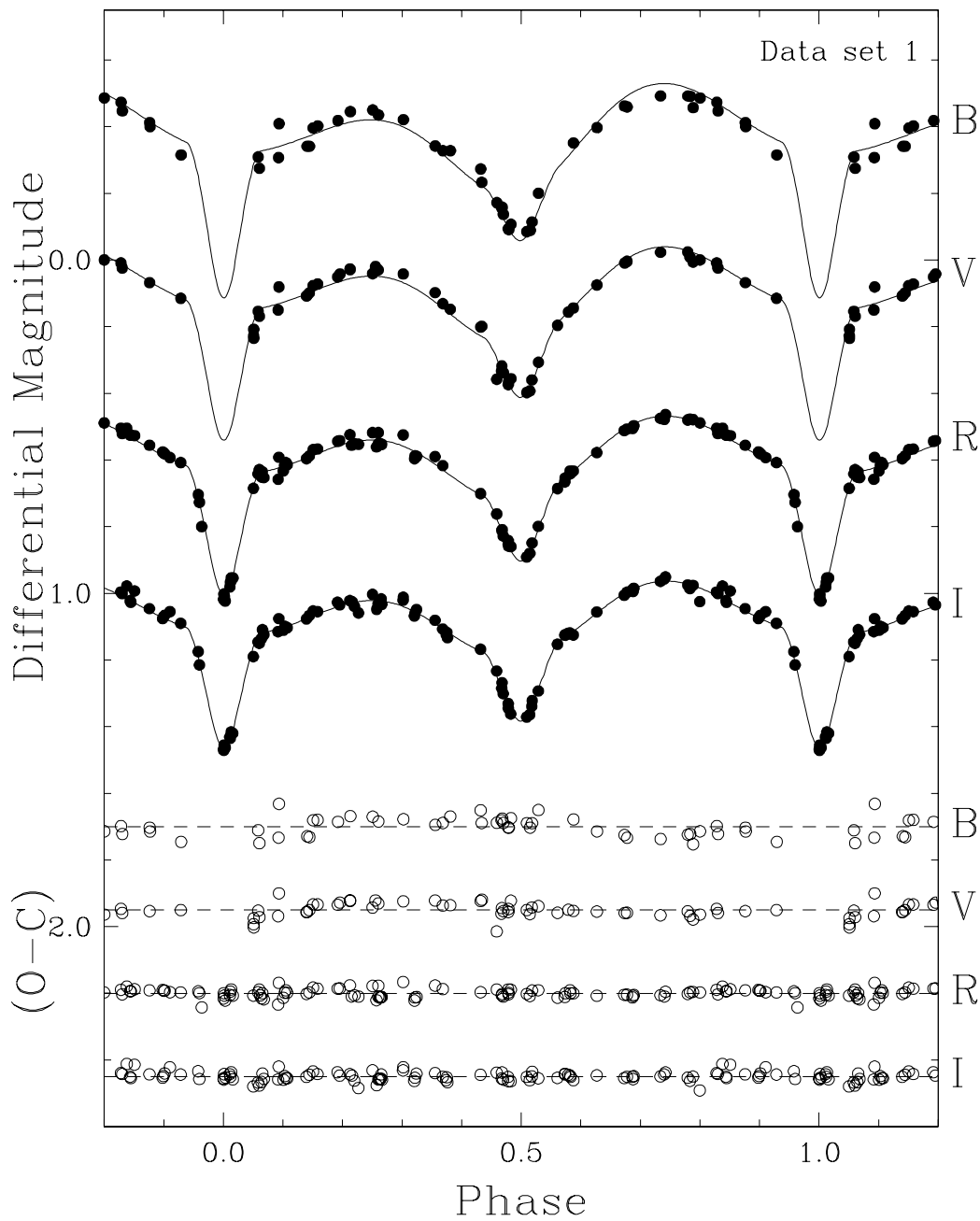


Fig. 2.— Photometric observations and light curve solutions for data set #1, computed from a simultaneous RI fit. The B and V observations, in which coverage of the primary minimum is lacking, were not used in the final solution (see text). The V , R , and I light curves are displaced vertically for display purposes. Residuals from the fits are shown at the bottom.

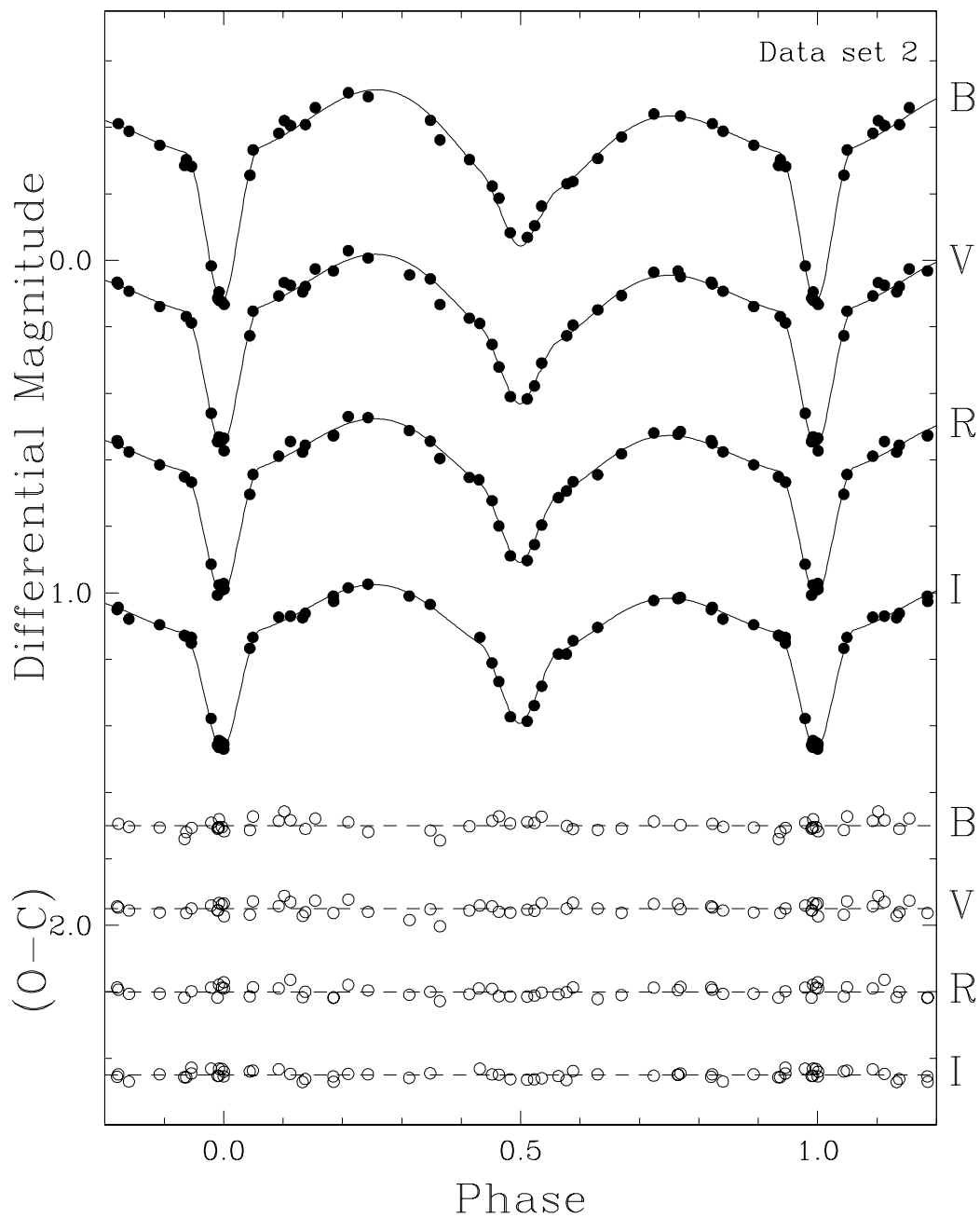
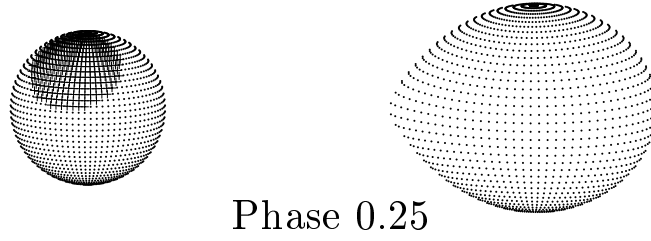


Fig. 3.— Photometric observations and light curve solutions for data set #2, computed from a simultaneous *BVRI* fit. The *V*, *R*, and *I* light curves are displaced vertically for display purposes. Residuals are shown at the bottom.

Data Set #1 (1997.1–1998.2)



Data Set #2 (1998.8–1999.2)

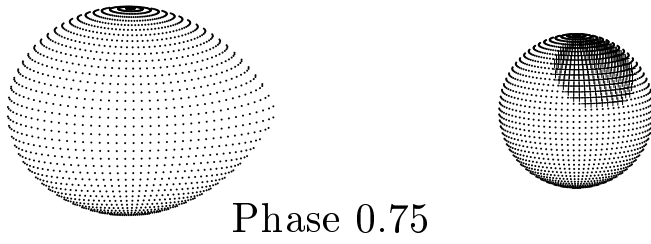


Fig. 4.— Representation of the cool spots on the primary star at the mean epoch of data sets #1 and #2. The size and separation of the stars are drawn to scale.

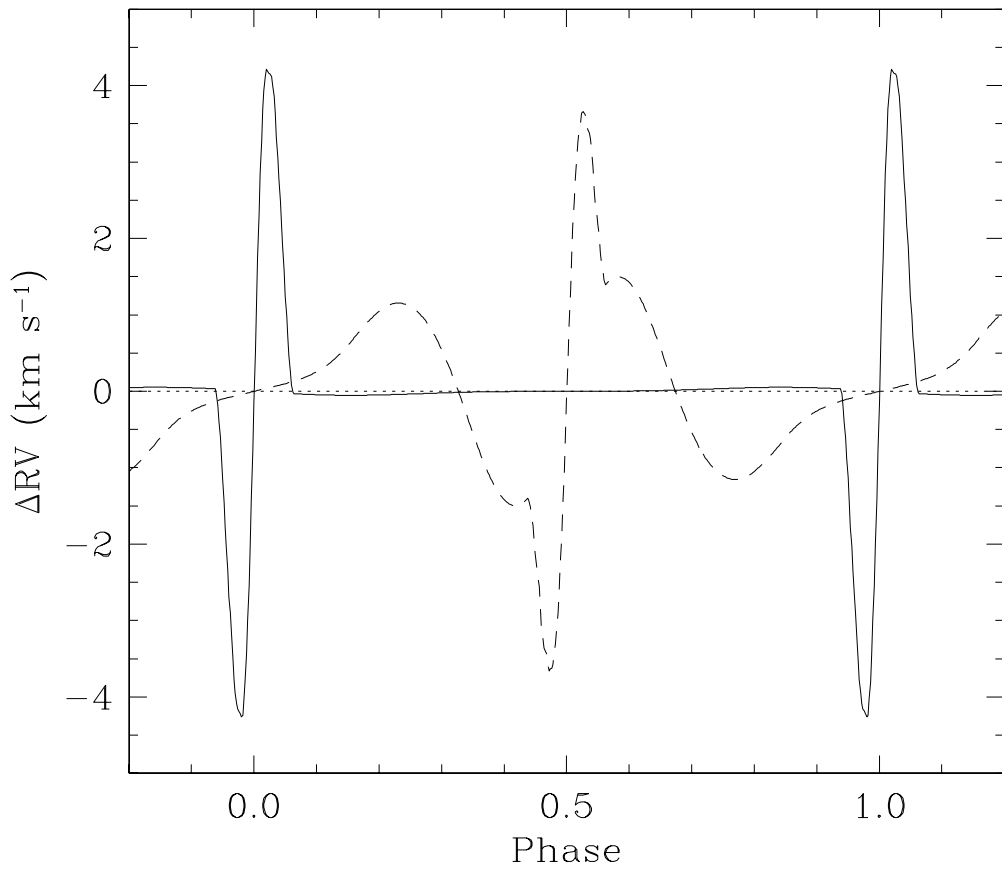


Fig. 5.— Effect of the distortions in the shape of the stars and the Rossiter effect on the measured radial velocities of the primary (solid curve) and secondary (dashed curve) of BD+05°706.

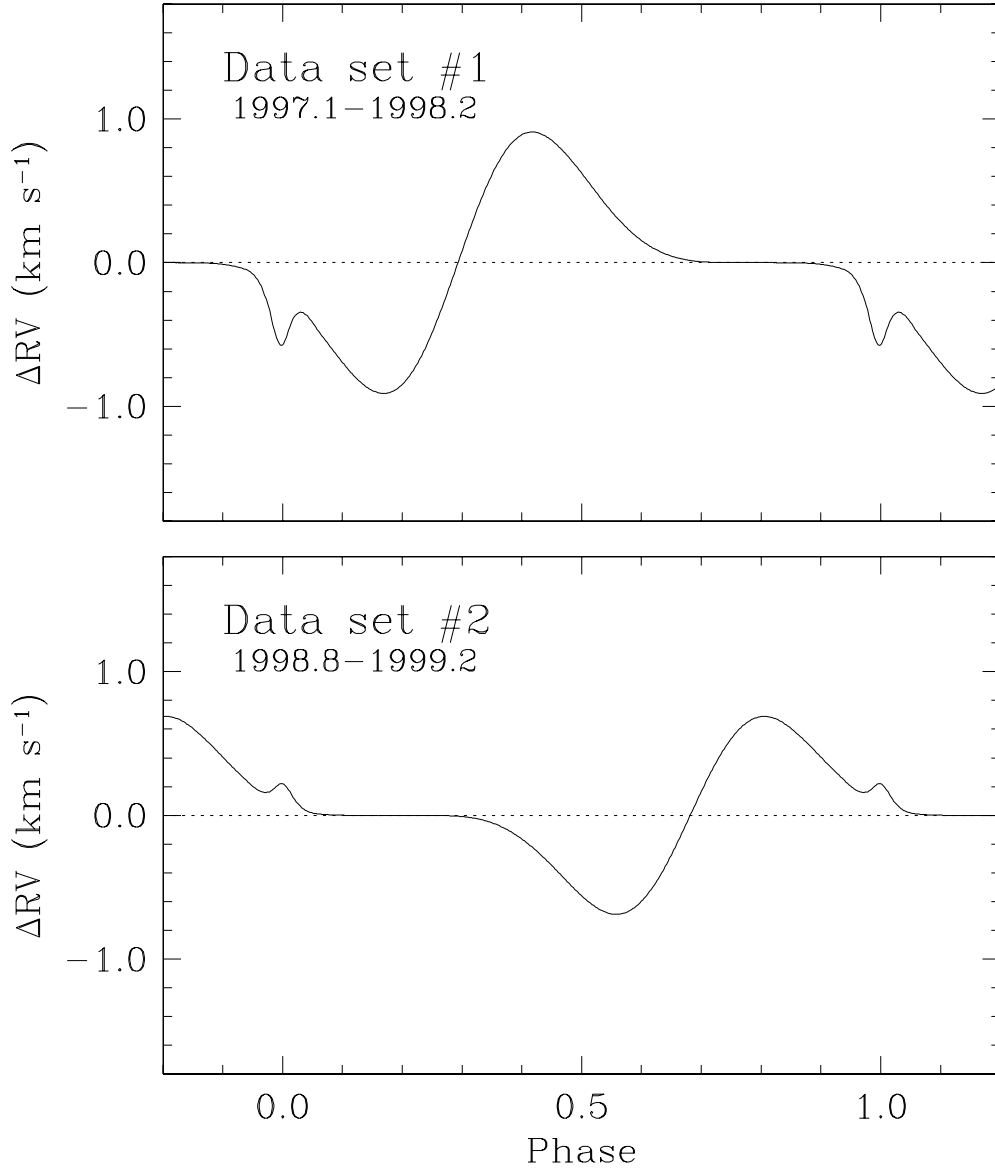


Fig. 6.— Effect of the spots on the primary of BD+05°706 upon the measured radial velocities of that component at the mean epoch of data sets #1 and #2.

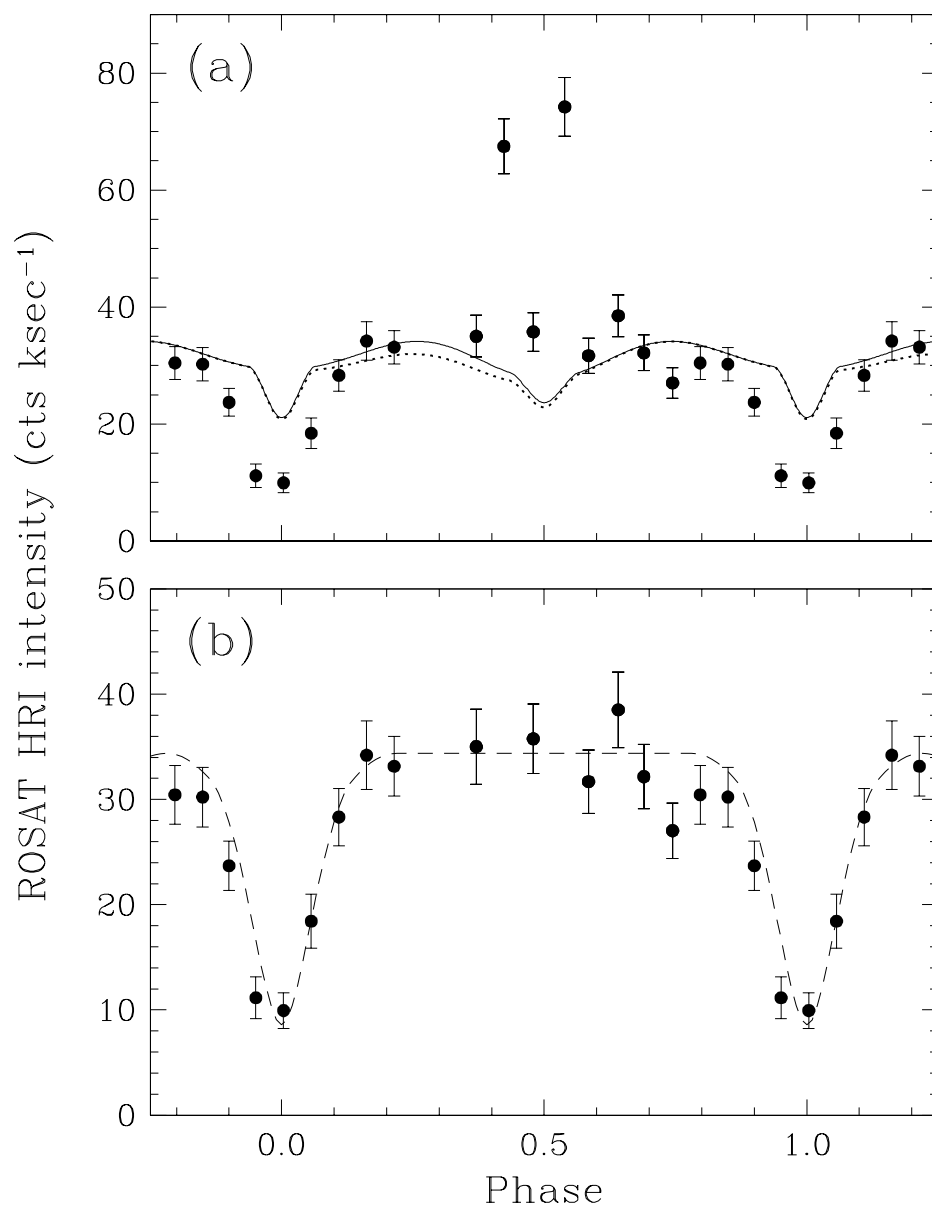


Fig. 7.— (a) ROSAT broad-band X-ray observations of BD+05°706 during a full orbital cycle, and optical light curve superimposed for comparison (R band from data set #1). The solid curve corresponds to the fit to the optical data with the distortions due to the cool spot removed, while the dotted curve includes the effect of the spot. The normalization is carried out at phase 0.75; (b) Toy model computed with the Wilson-Devinney code (see text) that provides a reasonably good match to the observed depth and duration of the primary eclipse (outliers near phase 0.5 ignored).

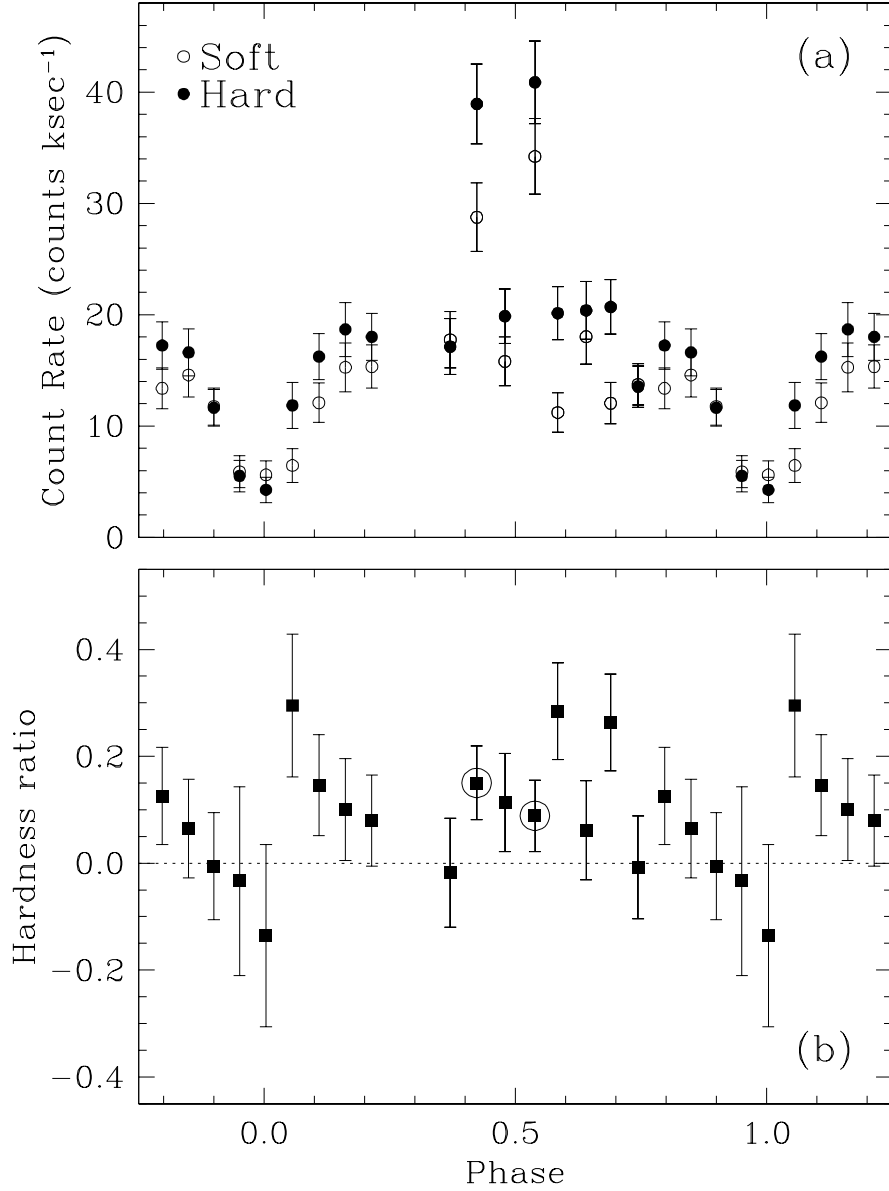


Fig. 8.— (a) ROSAT X-ray light curve of BD+05°706 separated into a soft band (0.1–0.5 keV) and a hard band (0.6–2.4 keV), as a function of orbital phase. (b) Hardness ratio (see text) for each ROSAT observation, as a function of phase. The two observations from the broad-band light curve (Figure 7) showing increased flux, possibly due to flares, are marked with circles.

Table 1. Program stars

Star	R.A. (J2000.0) Dec.	Sp.T.	V	$B-V$
BD+05°706	04 ^h 41 ^m 57.6 ^s +05°36'34''	G5	9.45	1.11
TYC 95-1495-1 (comparison)	04 ^h 41 ^m 36.0 ^s +05°43'10''		10.01	1.19
HD 29764 (check)	04 ^h 41 ^m 28.7 ^s +05°33'53''	F8	9.49	0.49

Table 2. Differential magnitudes in the B band, in the sense
 ⟨variable–comparison⟩.

HJD (2,450,000+)	ΔB (mag)	HJD (2,450,000+)	ΔB (mag)	HJD (2,450,000+)	ΔB (mag)	HJD (2,450,000+)	ΔB (mag)
772.6936	−0.412	827.7321	−0.457	903.5477	−0.486	1208.6844	−0.282
772.7038	−0.400	828.5234	−0.447	914.5239	−0.328	1209.5255	+0.113
773.6906	−0.315	834.5772	−0.396	915.5189	−0.233	1209.5601	+0.095
777.6886	−0.341	840.5560	−0.156	1133.7158	+0.017	1209.5601	+0.120
777.7616	−0.341	844.5362	−0.459	1136.7110	−0.408	1209.6537	+0.125
778.6654	−0.418	845.5979	−0.492	1140.6862	−0.421	1209.7217	+0.133
784.6604	−0.085	846.5413	−0.491	1142.6528	−0.223	1210.5415	−0.256
784.7649	−0.089	853.6187	−0.402	1148.6430	−0.434	1216.5883	−0.362
795.6793	−0.307	854.6542	−0.445	1149.6591	−0.411	1219.5979	−0.104
798.6679	−0.450	855.5462	−0.435	1157.6063	−0.492	1220.6234	−0.230
799.6417	−0.421	857.5909	−0.328	1162.6686	−0.069	1221.6098	−0.306
800.6508	−0.342	859.5101	−0.137	1165.6690	−0.371	1225.5947	−0.388
802.6055	−0.172	859.6675	−0.094	1166.6970	−0.440	1229.5403	−0.332
802.7780	−0.158	860.6232	−0.200	1170.6638	−0.285	1230.5336	−0.420
803.7220	−0.114	870.6699	−0.275	1173.6636	−0.382	1231.5202	−0.459
809.5834	−0.473	878.5792	−0.091	1180.6680	−0.187	1232.5722	−0.504
814.5945	−0.409	889.5291	−0.309	1190.6157	+0.114	1268.5297	−0.405
824.6819	−0.397	896.5880	−0.273	1198.6265	−0.303	1275.5187	−0.083
825.5523	−0.462	897.5484	−0.107	1207.6736	−0.346	1276.5165	−0.163
827.5643	−0.492	899.5315	−0.351	1208.5180	−0.303	1277.5134	−0.237

Table 3. Differential magnitudes in the V band, in the sense
 ⟨variable–comparison⟩.

HJD (2,450,000+)	ΔV (mag)	HJD (2,450,000+)	ΔV (mag)	HJD (2,450,000+)	ΔV (mag)	HJD (2,450,000+)	ΔV (mag)
772.6907	−0.432	827.5608	−0.524	899.5290	−0.356	1208.5156	−0.331
773.6792	−0.385	827.7283	−0.494	903.5449	−0.500	1208.6819	−0.312
777.6699	−0.392	828.5199	−0.476	914.5212	−0.352	1209.5229	+0.046
777.6784	−0.393	834.5746	−0.423	915.5230	−0.301	1209.5577	+0.031
777.7580	−0.401	840.5508	−0.167	1117.7249	−0.405	1209.6508	+0.041
778.6590	−0.449	840.5621	−0.182	1118.7028	−0.468	1209.7102	+0.035
784.6547	−0.102	842.6729	−0.344	1129.6644	−0.468	1209.7191	+0.073
784.7536	−0.107	844.5336	−0.496	1130.7223	−0.434	1210.5387	−0.273
785.6335	−0.304	845.5953	−0.523	1133.7128	−0.040	1215.6181	−0.456
795.6681	−0.350	846.5346	−0.508	1136.7083	−0.421	1216.5854	−0.367
797.6278	−0.458	853.6160	−0.428	1140.6837	−0.444	1219.5952	−0.122
798.6644	−0.459	854.6436	−0.473	1142.6502	−0.247	1220.6178	−0.273
798.7559	−0.480	854.6458	−0.471	1148.6445	−0.451	1221.6071	−0.351
799.6356	−0.458	855.5436	−0.470	1149.6565	−0.429	1225.5921	−0.407
800.6471	−0.402	857.5882	−0.369	1157.6036	−0.507	1229.5377	−0.347
802.6019	−0.142	859.5074	−0.162	1162.6661	−0.083	1230.5310	−0.433
803.7185	−0.140	859.6649	−0.126	1165.6664	−0.394	1231.5176	−0.474
809.5799	−0.491	860.6207	−0.193	1166.6945	−0.464	1232.5692	−0.529
813.7879	−0.273	870.6672	−0.331	1173.6611	−0.393	1268.5270	−0.425
813.7911	−0.292	878.5685	−0.134	1180.6655	−0.179	1274.5501	−0.310
813.7931	−0.265	889.5291	−0.346	1190.6129	+0.045	1275.5214	−0.090
814.5910	−0.419	896.5854	−0.299	1198.6206	−0.326	1276.5194	−0.191
824.6780	−0.425	897.5454	−0.144	1207.6708	−0.361	1277.5160	−0.305
825.5623	−0.491						

Table 4. Differential magnitudes in the R band, in the sense
 ⟨variable–comparison⟩.

HJD (2,450,000+)	ΔR (mag)	HJD (2,450,000+)	ΔR (mag)	HJD (2,450,000+)	ΔR (mag)	HJD (2,450,000+)	ΔR (mag)
474.5480	−0.417	528.5478	−0.346	824.6762	−0.472	1142.6482	−0.327
474.5930	−0.434	528.5859	−0.323	825.5468	−0.538	1148.6430	−0.535
474.6310	−0.442	529.5529	−0.069	827.5594	−0.570	1149.6551	−0.500
474.6720	−0.436	529.5683	−0.083	827.7268	−0.571	1157.6019	−0.577
477.5058	−0.489	529.5919	−0.096	828.5184	−0.529	1162.6646	−0.147
477.5638	−0.499	530.5133	−0.406	834.5729	−0.481	1163.6604	−0.336
477.6088	−0.496	530.5567	−0.399	840.5600	−0.238	1165.6650	−0.468
477.6338	−0.497	530.5831	−0.414	844.5315	−0.543	1166.6930	−0.531
477.6518	−0.497	546.5490	−0.457	845.5935	−0.575	1170.6589	−0.399
477.6718	−0.497	547.5586	−0.250	846.5327	−0.573	1173.6598	−0.461
483.4803	−0.384	548.5461	−0.096	853.6143	−0.483	1180.6640	−0.251
483.4933	−0.396	549.5267	−0.397	854.6396	−0.526	1190.6113	−0.043
483.6473	−0.417	552.5314	−0.497	855.5412	−0.532	1198.6206	−0.397
483.6563	−0.409	772.6879	−0.494	857.5866	−0.433	1207.6685	−0.435
489.6607	−0.470	773.6775	−0.442	859.5056	−0.222	1208.6799	−0.383
489.6847	−0.469	777.6683	−0.454	859.6624	−0.208	1209.5563	−0.074
491.5536	−0.032	777.7565	−0.462	859.6700	−0.192	1209.6492	−0.059
491.5636	−0.048	778.6568	−0.506	860.6190	−0.251	1209.7085	−0.078
491.5736	−0.041	784.6533	−0.159	870.6653	−0.421	1209.7176	−0.061
491.6055	−0.027	784.7522	−0.170	878.5668	−0.197	1210.5372	−0.346
497.6100	−0.454	785.6314	−0.364	889.5257	−0.408	1215.6097	−0.538
497.6280	−0.462	795.6657	−0.392	896.5838	−0.349	1216.5839	−0.454
497.6800	−0.461	797.6207	−0.508	897.5429	−0.190	1219.5937	−0.195
504.5271	−0.544	798.6629	−0.532	899.5276	−0.417	1220.6126	−0.356
504.5450	−0.549	799.6332	−0.525	903.5432	−0.561	1221.6048	−0.405
504.5686	−0.553	800.6455	−0.460	1117.7233	−0.473	1225.5905	−0.474
505.5372	−0.572	802.6005	−0.288	1118.7001	−0.522	1229.5362	−0.406
505.5740	−0.586	802.7744	−0.241	1118.7126	−0.524	1232.5674	−0.580
507.4900	−0.525	803.7233	−0.201	1129.6626	−0.527	1268.5255	−0.505
507.5100	−0.524	809.5782	−0.545	1130.7208	−0.508	1274.5253	−0.390
507.6310	−0.523	809.7652	−0.545	1133.7111	−0.136	1275.5227	−0.161
508.5222	−0.474	813.7806	−0.365	1136.7057	−0.494	1276.5209	−0.254
514.5140	−0.494	814.5891	−0.458	1140.6819	−0.506	1277.5194	−0.384
514.6029	−0.499						

Table 5. Differential magnitudes in the I band, in the sense
 \langle variable–comparison \rangle .

HJD (2,450,000+)	ΔI (mag)	HJD (2,450,000+)	ΔI (mag)	HJD (2,450,000+)	ΔI (mag)	HJD (2,450,000+)	ΔI (mag)
474.5550	−0.489	514.5256	−0.575	814.5870	−0.524	1140.6806	−0.565
474.5950	−0.501	514.6011	−0.561	824.6744	−0.544	1142.6471	−0.389
474.6380	−0.497	528.5456	−0.425	825.5444	−0.594	1148.6419	−0.586
474.6740	−0.497	528.5838	−0.385	827.5575	−0.625	1149.6539	−0.556
477.5108	−0.552	529.5488	−0.169	827.7251	−0.624	1157.6004	−0.626
477.5908	−0.571	529.5664	−0.165	828.5168	−0.599	1162.6634	−0.214
477.6108	−0.569	529.5902	−0.184	834.5717	−0.547	1163.6587	−0.416
477.6368	−0.571	530.5581	−0.465	840.5587	−0.315	1166.6909	−0.577
477.6558	−0.583	530.5850	−0.491	842.6694	−0.480	1170.6574	−0.472
477.6758	−0.567	546.5476	−0.545	844.5297	−0.603	1173.6584	−0.527
483.4833	−0.474	548.5441	−0.180	845.5922	−0.636	1180.6629	−0.333
483.4903	−0.476	549.5287	−0.476	846.5297	−0.614	1190.6102	−0.142
483.6453	−0.481	552.5296	−0.541	853.6131	−0.545	1190.6541	−0.135
483.6603	−0.478	772.6852	−0.554	854.6380	−0.578	1198.9575	−0.466
489.6417	−0.528	773.6760	−0.510	855.5386	−0.569	1207.6672	−0.504
489.6827	−0.534	777.6661	−0.523	857.5851	−0.493	1208.5128	−0.469
491.5516	−0.132	777.7550	−0.533	859.5043	−0.299	1208.6774	−0.449
491.5616	−0.129	778.6511	−0.573	859.6609	−0.269	1208.6787	−0.466
491.5716	−0.145	784.6513	−0.229	860.6173	−0.307	1209.5551	−0.156
491.6105	−0.137	784.7507	−0.236	870.6636	−0.450	1209.6478	−0.150
497.6050	−0.532	785.6289	−0.447	878.5655	−0.255	1209.7063	−0.130
497.6250	−0.541	795.6635	−0.485	889.5226	−0.454	1209.7164	−0.145
497.6740	−0.551	797.6187	−0.565	896.5817	−0.432	1210.5362	−0.433
498.6169	−0.476	798.6614	−0.597	897.5411	−0.238	1215.6081	−0.590
498.6339	−0.483	799.6308	−0.579	899.5256	−0.475	1219.5845	−0.261
498.6569	−0.467	799.6353	−0.588	903.5375	−0.575	1220.6091	−0.416
504.5253	−0.611	800.6440	−0.519	1117.7217	−0.525	1221.6032	−0.496
504.5426	−0.605	802.5989	−0.367	1118.6984	−0.590	1225.5884	−0.521
504.5669	−0.615	802.7705	−0.332	1118.7112	−0.574	1229.5347	−0.466
505.5347	−0.643	803.7137	−0.261	1129.6608	−0.583	1232.5661	−0.615
505.5722	−0.649	803.7275	−0.278	1129.6707	−0.583	1268.5243	−0.530
507.4912	−0.578	809.5767	−0.604	1130.7195	−0.550	1275.5238	−0.227
507.5083	−0.573	809.7627	−0.622	1133.7098	−0.222	1276.5225	−0.319
507.6290	−0.607	813.7789	−0.410	1136.7032	−0.538	1277.5205	−0.456
508.5199	−0.524						

Table 6. ROSAT X-ray observations of BD+05°706.

HJD (2,400,000+)	Exposure (s)	Soft band (0.1–0.5 keV)			Hard band (0.6–2.4 keV)			Broad band (0.1–2.4 keV)			HR^b	σ_{HR}	Phase
		Counts	Error	ML^a	Counts	Error	ML^a	Counts	Error	ML^a			
50678.6448	4456	52.43	7.42	165.2	51.85	7.38	143.7	104.14	10.47	299.2	−0.01	0.10	0.900
50679.6073	2940	17.34	4.24	61.8	16.22	4.15	43.2	32.98	5.90	101.3	−0.03	0.18	0.951
50680.6024	3621	20.34	4.57	64.3	15.48	4.10	32.2	35.65	6.13	91.4	−0.14	0.17	0.004
50681.6007	2871	18.55	4.36	62.0	34.06	5.95	108.1	52.60	7.38	169.8	+0.29	0.13	0.056
50682.5965	3969	48.01	7.03	176.5	64.45	8.16	195.2	112.64	10.78	370.0	+0.15	0.09	0.109
50683.5920	3262	49.84	7.11	224.7	60.94	7.89	227.6	111.23	10.64	443.0	+0.10	0.10	0.162
50684.5872	4190	64.31	8.10	254.5	75.47	8.79	260.0	139.26	11.94	508.8	+0.08	0.09	0.214
50687.5392	2783	49.43	7.07	196.7	47.69	6.97	161.8	97.25	9.94	349.3	−0.02	0.10	0.371
50688.5344 ^c	3066	88.18	9.43	434.4	119.38	10.99	497.5	207.54	14.49	928.3	+0.15	0.07	0.423
50689.5924	3351	52.98	7.33	232.9	66.57	8.24	242.0	119.40	11.02	470.5	+0.11	0.09	0.479
50690.7236 ^c	2993	102.41	10.15	490.3	122.37	11.12	530.9	224.66	15.06	1015.0	+0.09	0.07	0.539
50691.5826	3615	40.56	6.41	173.4	72.82	8.64	237.2	113.82	10.81	409.3	+0.28	0.09	0.585
50692.6469	3087	55.64	7.53	220.6	62.93	8.03	212.1	118.36	11.01	427.8	+0.06	0.09	0.641
50693.5719	3521	42.45	6.56	169.2	72.87	8.62	241.5	114.89	10.82	407.0	+0.26	0.09	0.690
50694.6045	4054	55.74	7.54	164.9	54.91	7.53	175.6	110.07	10.65	333.2	−0.01	0.10	0.745
50695.5993	4000	53.56	7.39	187.0	68.96	8.47	199.5	123.10	11.26	379.6	+0.13	0.09	0.797
50696.5934	3850	56.17	7.58	187.5	63.95	8.11	187.0	119.43	11.07	373.3	+0.06	0.09	0.850

^aMaximum Likelihood estimator (see text).

^bHardness ratio (see text).

^cPossible flare.

Table 7. Parameters of the light curve solutions for data set #1

Parameter	<i>R</i> Solution	<i>I</i> Solution	<i>RI</i> Solution
Geometric and radiative parameters			
<i>i</i> (°) ^a	79.55 ± 0.18	79.46 ± 0.15	79.470 ± 0.074
<i>q</i> ≡ <i>M</i> ₂ / <i>M</i> ₁	0.2055	0.2055	0.2055
Ω ₁ ^a	6.05 ± 0.25	5.89 ± 0.16	6.03 ± 0.10
Ω ₂	2.246 ± 0.011	2.246 ± 0.011	2.246 ± 0.011
<i>r</i> _{point} (primary, secondary) ..	0.1718 , 0.3439	0.1767 , 0.3439	0.1724 , 0.3439
<i>r</i> _{pole} (primary, secondary) ..	0.1710 , 0.2348	0.1758 , 0.2348	0.1716 , 0.2348
<i>r</i> _{side} (primary, secondary) ..	0.1715 , 0.2442	0.1764 , 0.2442	0.1721 , 0.2442
<i>r</i> _{back} (primary, secondary) ..	0.1718 , 0.2767	0.1768 , 0.2767	0.1724 , 0.2767
<i>r</i> _{vol} ^b (primary, secondary) ...	0.1714 , 0.2513	0.1763 , 0.2513	0.1720 , 0.2513
Δ <i>φ</i>	−0.00006 ± 0.00058	+0.00097 ± 0.00064	+0.00040 ± 0.00040
<i>T</i> ₁ (K)	5000	5000	5000
<i>T</i> ₂ (K) ^a	4612 ± 47	4677 ± 40	4638 ± 11
<i>L</i> _{1,<i>R</i>} ^c	0.3956 ± 0.0091	...	0.3911 ± 0.0004
<i>L</i> _{1,<i>I</i>} ^c	0.3810 ± 0.0077	0.3764 ± 0.0004
Albedo	0.5 , 0.5	0.5 , 0.5	0.5 , 0.5
Gravity brightening	0.365 , 0.365	0.365 , 0.365	0.365 , 0.365
Spot parameters (primary star)			
<i>l</i> (°)	257.77 ± 0.09	254.44 ± 0.11	254.39 ± 0.04
<i>b</i> (°)	45	45	45
<i>r</i> (°)	36.33 ± 1.35	37.29 ± 1.63	37.05 ± 0.28
<i>TF</i> ^d	0.84	0.84	0.84
Limb darkening coefficients (linear law)			
<i>x</i> _{1,<i>R</i>}	0.589	...	0.589
<i>x</i> _{1,<i>I</i>}	0.481	0.481
<i>x</i> _{1,bolo}	0.527	0.527	0.527
<i>x</i> _{2,<i>R</i>}	0.639	...	0.635
<i>x</i> _{2,<i>I</i>}	0.511	0.515
<i>x</i> _{2,bolo}	0.528	0.527	0.528
Other quantities pertaining to the fit			
σ _{<i>R</i>} (mag)	0.0126	...	0.0127
σ _{<i>I</i>} (mag)	0.0131	0.0133
<i>N</i> _{obs}	92	95	187

^aFixed in the combined solution (see text).

^bRelative radius of a sphere with the same volume as the distorted star.

^cFractional luminosity of the primary.

^dFixed temperature factor (*T*_{spot}/*T*_{star}).

Table 8. Parameters of the light curve solutions for data set #2

Parameter	<i>B</i> Solution	<i>V</i> Solution	<i>R</i> Solution	<i>I</i> Solution	<i>BVRI</i> Solution
Geometric and radiative parameters					
i ($^{\circ}$) ^a	79.24 ± 0.21	79.41 ± 0.25	79.38 ± 0.36	79.55 ± 0.30	79.470 ± 0.074
$q \equiv M_2/M_1$	0.2055	0.2055	0.2055	0.2055	0.2055
Ω_1 ^a	6.39 ± 0.53	5.83 ± 0.34	5.83 ± 0.35	6.07 ± 0.32	6.03 ± 0.10
Ω_2	2.246 ± 0.011	2.246 ± 0.011	2.246 ± 0.011	2.246 ± 0.011	2.246 ± 0.011
r_{point} (primary, secondary) ..	0.1623 , 0.3439	0.1787 , 0.3439	0.1787 , 0.3439	0.1712 , 0.3439	0.1724 , 0.3439
r_{pole} (primary, secondary) ..	0.1616 , 0.2348	0.1777 , 0.2348	0.1777 , 0.2348	0.1704 , 0.2348	0.1716 , 0.2348
r_{side} (primary, secondary) ..	0.1620 , 0.2442	0.1783 , 0.2442	0.1783 , 0.2442	0.1710 , 0.2442	0.1721 , 0.2442
r_{back} (primary, secondary) ..	0.1622 , 0.2767	0.1786 , 0.2767	0.1786 , 0.2767	0.1712 , 0.2767	0.1724 , 0.2767
r_{vol} ^b (primary, secondary) ...	0.1620 , 0.2513	0.1782 , 0.2513	0.1782 , 0.2513	0.1709 , 0.2513	0.1720 , 0.2513
$\Delta\phi$	-0.0025 ± 0.0011	-0.00331 ± 0.00096	-0.00329 ± 0.00088	-0.00201 ± 0.00077	-0.00272 ± 0.00044
T_1 (K)	5000	5000	5000	5000	5000
T_2 (K) ^a	4565 ± 67	4671 ± 52	4715 ± 56	4701 ± 59	4638 ± 11
$L_{1,B}$ ^c	0.443 ± 0.013	0.4353 ± 0.0007
$L_{1,V}$ ^c	0.418 ± 0.016	0.4102 ± 0.0006
$L_{1,R}$ ^c	0.390 ± 0.020	...	0.3911 ± 0.0006
$L_{1,I}$ ^c	0.361 ± 0.015	0.3764 ± 0.0007
Albedo	0.5 , 0.5	0.5 , 0.5	0.5 , 0.5	0.5 , 0.5	0.5 , 0.5
Gravity brightening	0.365 , 0.365	0.365 , 0.365	0.365 , 0.365	0.365 , 0.365	0.365 , 0.365
Spot parameters (primary star)					
l ($^{\circ}$)	110.29 ± 0.17	113.14 ± 0.14	117.81 ± 0.14	112.06 ± 0.14	112.73 ± 0.07
b ($^{\circ}$)	45	45	45	45	45
r ($^{\circ}$)	35.0 ± 1.2	33.0 ± 2.0	33.4 ± 2.2	34.7 ± 1.6	33.83 ± 0.65
T_{F}^{d}	0.87	0.87	0.87	0.87	0.87
Limb darkening coefficients (linear law)					
$x_{1,B}$	0.867	0.867
$x_{1,V}$	0.714	0.714
$x_{1,R}$	0.589	...	0.589
$x_{1,I}$	0.481	0.481
$x_{1,\text{bolo}}$	0.527	0.527	0.527	0.527	0.527
$x_{2,B}$	0.944	0.931
$x_{2,V}$	0.768	0.774
$x_{2,R}$	0.624	...	0.635
$x_{2,I}$	0.508	0.515
$x_{2,\text{bolo}}$	0.529	0.527	0.527	0.527	0.528
Other quantities pertaining to the fit					
σ_B (mag)	0.0169	0.0180
σ_V (mag)	0.0167	0.0171
σ_R (mag)	0.0134	...	0.0145
σ_I (mag)	0.0104	0.0112
N_{obs}	37	42	41	42	162

^aFixed in the combined solution (see text).

^bRelative radius of a sphere with the same volume as the distorted star.

^cFractional luminosity of the primary.

^dFixed temperature factor ($T_{\text{spot}}/T_{\text{star}}$).

Table 9. Revised radial velocity measurements of BD+05°706, and residuals from the spectroscopic orbit.

HJD (2,400,000+)	RV_1^{obs} ^a (km s^{-1})	RV_2^{obs} ^a (km s^{-1})	ΔRV_1 ^b (km s^{-1})	ΔRV_2 ^b (km s^{-1})	RV_1 ^c (km s^{-1})	RV_2 ^c (km s^{-1})	(O-C) ₁ (km s^{-1})	(O-C) ₂ (km s^{-1})	Orbital phase
(1)	(2)	(3)	(4)	(5)	(6)	(7)	(8)	(9)	(10)
49437.5420 . . .	-33.96	+79.12	-0.04	+1.16	-34.00	+80.28	+2.91	+2.70	0.229
49614.0033 . . .	-10.38	-55.19	0.00	+1.44	-10.38	-53.75	-0.95	+2.34	0.567
49644.9114 . . .	-37.77	+72.73	-0.05	+1.06	-37.82	+73.79	-1.64	-0.24	0.202
49648.9088 . . .	-27.64	+35.10	-0.00	-1.50	-27.64	+33.60	-0.04	+1.27	0.413
49653.8368 . . .	+1.52	-101.99	+0.02	-0.03	+1.54	-102.02	+1.44	+0.43	0.674
49680.9384 . . .	-29.45	+43.32	-0.05	+0.30	-29.50	+43.62	+0.24	+0.89	0.108
49681.7665 . . .	-33.04	+60.85	-0.05	+0.62	-33.09	+61.47	+0.36	+0.73	0.152
49696.7771 . . .	-9.42	-46.10	-0.76	-0.11	-10.18	-46.21	+0.66	+3.04	0.946
49700.7398 . . .	-33.59	+59.35	-0.05	+0.67	-33.64	+60.02	+0.08	-2.07	0.156
49704.7351 . . .	-34.58	+53.31	-0.01	-0.94	-34.59	+52.37	-2.61	-1.25	0.367
49708.6896 . . .	-8.72	-63.23	0.00	+1.49	-8.72	-61.74	-0.42	-0.12	0.576
49732.7773 . . .	-1.03	-93.39	+0.05	-0.59	-0.98	-93.98	+0.54	+0.58	0.851
49734.8029 . . .	-9.50	-40.34	-2.56	-0.08	-12.06	-40.42	+0.20	+1.88	0.958
49766.6378 . . .	-1.68	-92.32	+0.01	+0.71	-1.67	-91.61	+0.34	+0.59	0.643
49767.6563 . . .	+0.53	-109.05	+0.02	-0.49	+0.55	-109.54	-0.65	-1.71	0.697
49815.6120 . . .	-37.30	+78.13	-0.04	+1.15	-37.34	+79.28	-0.36	+1.35	0.234
49964.0085 . . .	-27.93	+30.63	-0.04	+0.20	-27.97	+30.83	-0.43	-1.17	0.086
49969.9892 . . .	-29.01	+39.59	0.00	-1.44	-29.01	+38.15	-0.32	+0.53	0.403
49971.0119 . . .	-24.69	+8.75	0.00	-2.71	-24.69	+6.04	-2.02	-2.27	0.457
50002.9115 . . .	-35.21	+57.25	-0.05	+0.55	-35.26	+57.80	-2.34	-0.40	0.145
50006.9548 . . .	-32.05	+58.81	-0.01	-0.75	-32.06	+58.06	+0.61	+1.11	0.359
50031.9081 . . .	-0.28	-104.85	+0.02	-0.12	-0.26	-104.97	-0.64	-1.16	0.679
50033.8891 . . .	+2.26	-110.16	+0.04	-1.13	+2.30	-111.29	+0.44	-0.26	0.784
50051.7831 . . .	+2.68	-110.90	+0.03	-0.97	+2.71	-111.87	+0.55	+0.61	0.731
50060.8041 . . .	-35.47	+74.57	-0.05	+1.10	-35.52	+75.67	+0.88	+0.57	0.208
50061.7975 . . .	-37.73	+77.49	-0.03	+1.04	-37.76	+78.53	-0.73	+0.33	0.261
50062.7964 . . .	-35.10	+71.98	-0.02	+0.28	-35.12	+72.26	+0.41	+1.35	0.313
50064.6757 . . .	-27.02	+35.36	-0.00	-1.49	-27.02	+33.87	+0.62	+1.38	0.413
50083.6864 . . .	-26.41	+33.18	-0.00	-1.50	-26.41	+31.68	+0.59	+2.27	0.419
50085.7517 . . .	-13.29	-35.19	0.00	+3.64	-13.29	-31.55	+0.64	+2.64	0.528
50088.7862 . . .	+0.62	-105.51	+0.02	-0.32	+0.64	-105.83	-0.22	+0.32	0.689
50090.7706 . . .	+1.38	-107.20	+0.05	-1.09	+1.43	-108.29	-0.14	+1.32	0.794
50092.7725 . . .	-5.88	-73.48	+0.05	-0.26	-5.83	-73.74	-0.06	+0.17	0.900
50117.6706 . . .	-36.09	+75.44	-0.04	+1.13	-36.13	+76.57	+0.53	+0.21	0.217
50141.6862 . . .	-19.15	-12.00	0.00	-2.62	-19.15	-14.62	-0.25	-4.60	0.488
50143.6293 . . .	-7.21	-70.78	-0.00	+1.48	-7.21	-69.30	-0.43	-0.29	0.591
50144.6373 . . .	-3.42	-93.00	+0.01	+0.70	-3.41	-92.30	-1.50	+0.38	0.644
50145.6448 . . .	+1.11	-107.04	+0.02	-0.48	+1.13	-107.52	-0.10	+0.45	0.697
50148.6641 . . .	-3.71	-91.19	+0.05	-0.54	-3.66	-91.73	-1.68	+0.62	0.857
50149.5956 . . .	-6.31	-69.74	+0.04	-0.23	-6.27	-69.97	+0.18	+0.63	0.906
50153.6415 . . .	-31.32	+45.86	-0.05	+0.36	-31.37	+46.22	-0.47	-2.13	0.120

^aMeasured velocities, including the corrections described in the text to account for the effect of the narrow spectral window.

^bCombined corrections due to proximity and to the Rossiter effect (see text), to be added to the measured velocities.

^cFinal velocities used for the orbital solution.

Table 10. Spectroscopic orbital elements of
BD+05°706.

Parameter	Value
P (days)	18.8988 ± 0.0011
γ (km s^{-1})	-17.39 ± 0.14
K_1 (km s^{-1})	19.69 ± 0.22
K_2 (km s^{-1})	95.80 ± 0.33
e	0 (fixed)
T_{max} (HJD) ^a	$2,449,919.857 \pm 0.011$
$a_1 \sin i$ (10^6 km)	5.117 ± 0.059
$a_2 \sin i$ (10^6 km)	24.897 ± 0.088
$a \sin i$ (R_{\odot})	43.12 ± 0.15
$M_1 \sin^3 i$ (M_{\odot})	2.502 ± 0.026
$M_2 \sin^3 i$ (M_{\odot})	0.5143 ± 0.0085
$q \equiv M_2/M_1$	0.2055 ± 0.0025
N_{obs}	41
σ_1 (km s^{-1})	1.05
σ_2 (km s^{-1})	1.57

^aTime of maximum primary velocity.

Table 11. Summary of system parameters for BD+05°706.

Parameter	Primary	Secondary
P (days)	18.8988 ± 0.0011	
a (R_{\odot})	43.86 ± 0.15	
M (M_{\odot})	2.633 ± 0.028	0.5412 ± 0.0093
R (R_{\odot})	7.55 ± 0.20	11.02 ± 0.21
T (K)	5000 ± 100	4640 ± 150
$\log g$	3.103 ± 0.023	2.087 ± 0.018
$\bar{\rho}$ (10^{-3} g cm $^{-3}$) ^a	8.63 ± 0.68	0.569 ± 0.034
$v_{\text{sync}} \sin i$ (km s $^{-1}$) ^b	19.9 ± 0.5	29.0 ± 0.6
$v \sin i$ (km s $^{-1}$) ^c	23 ± 1	31 ± 2
$\log L_{\text{bol}}$ (L_{\odot})	1.504 ± 0.041	1.704 ± 0.059
$\log L_X$ (ergs s $^{-1}$)	31.96 ± 0.07	
L_2/L_1	1.58 ± 0.27	
M_{bol} (mag)	0.97 ± 0.10	0.47 ± 0.15
M_V (mag)	1.26 ± 0.11	0.98 ± 0.18
$m - M$ (mag)	8.87 ± 0.18	
Distance (pc)	595 ± 51	

^aMean stellar density.

^bProjected rotational velocity based on the radius and the period, assuming synchronous rotation.

^cSpectroscopically measured rotational velocity.